Controlling heat capacity in a thermal concentrator using metamaterials: numerical and experimental studies

Thiwanka Arepolage [a], Christophe Verdy [b], Thibaut Sylvestre [a], Aymeric Leray [c], Sébastien Euphrasie [a,*]

[a] *Université de Franche-Comté, CNRS, institut FEMTO-ST, Besançon, France*

[b] *UTBM, CNRS, laboratoire ICB - LERMPS, Belfort, France*

[c] *Université de Bourgogne, CNRS, laboratoire ICB, Dijon France*

Abstract

We developed two thermal concentrators, one with a 2D design of uniform thickness and another with a 3D design, using the coordinate transformation technique and metamaterials. By structuring the thermal conductor, we were able to achieve the desired local density-heat capacity product ρC and anisotropic thermal conductivities. Homogenized thermal conductivities were obtained from the boundary heat fluxes of the unit cells computed with finite element simulations and taking into account the cylindrical symmetry. We fabricated the 3D concentrator using 3D metal printing and used a thermal camera for characterization. By designing the unit cells to obtain the (ρC) values given by the coordinate transformation, the time evolution characteristics of the metadevice are closer to those of an ideal concentrator when compared to devices that solely consider anisotropic conductivities.

Keywords: Metamaterial; Thermal metadevice; Effective medium; Thermal conductivity; Heat capacity

1. Introduction

Metamaterials are engineered materials designed to possess properties that are rarely observed in nature such as negative refractive index [1, 2] or negative Poisson ratio [3]. They are typically composite materials structured on a scale much smaller than the relevant dimension (e.g. the wavelength of the propagating waves). They have gained popularity for their applications in various domains, such as electromagnetics [4], acoustics [5], thermal [6]. In the field of manipulating heat flow, metamaterials have been proposed for numerous applications such as thermal cloaks [7, 8, 9, 10], thermal concentrators [7, 8, 11], heat flux reversers [8], macroscopic thermal diodes [12] and thermal encoding [13] among others. One of the tools to design such metamaterials is transformation thermodynamics [7, 14, 15]. It leads to position dependent density-heat capacity product and anisotropic thermal conductivities. Thermal cloaks [6, 16] and thermal concentrators [17, 18, 19, 20, 21] have already been experimentally demonstrated and tested. However, they only considered the desired thermal conductivities but not the density-heat capacity product ρC, which is crucial for non-steady state applications.

In this paper, we propose a methodology for incorporating the density-heat capacity product in the design of such devices. We specifically focus on a thermal concentrator, but our approach can be applied to other applications utilizing the coordinate transformations. The classical method of discretization has been employed to achieve position dependent properties. In contrast to previous works [17], we did not use the two-scale homogenization theory to calculate the homogenized thermal properties; we instead used an approach based on boundary fluxes, while considering the circular symmetry. The ρC product was adjusted by adding material in regions where it

[1] sebastien.euphrasie@femto-st.fr

has minimal impact on heat flow. Here, we present two examples: one with a constant thickness and one with a varying thickness. To demonstrate the feasibility and effectiveness of our designs, we fabricated the second design using 3D metal printing. We characterized it and compared the results with finite element (FE) simulations.

The subsequent sections of this paper are structured as follows. Section 2 describes the methodology used in our design process. It begins with a brief overview of the coordinate transformation principle applied to a concentrator using a linear function. Next, we present our approach for computing the homogenized anisotropic thermal conductivities and the homogenized ρC of a unit cell of our metadevice. We then explain the two different methodologies (2D and 3D) used to not only obtain the desired local anisotropic conductivities but also the desired local density-heat capacity product ρC. The fabrication process and characterization are also presented in section 2. Section 3 presents the results, including a comparison between simulations and experimental results.

2. Methods

2.1. Coordinate transformation

Let us consider the two-dimensional transformation $(r', \theta') = (f(r), \theta)$ in polar coordinates. The heat equation resulting from this transformation applied to a homogeneous isotropic material can maintain its form as:

$$\nabla \cdot \left(\bar{\bar{K}}' \nabla T\right) = \rho C' \frac{\partial T}{\partial t}, \tag{1}$$

with T the temperature, t the time, $\bar{\bar{K}}'$ the transformed conductivity tensor and $\rho C'$ the transformed density-heat capacity product written as [7, 9]

$$\bar{\bar{K}}' = K\, R(\theta) \begin{pmatrix} K'_{rr} & 0 \\ 0 & K'_{\theta\theta} \end{pmatrix} R(\theta)^T, \tag{2}$$

$$K'_{rr}(r') = \frac{g(r')}{r' \frac{dg}{dr'}(r')}, \quad K'_{\theta\theta} = \frac{1}{K'_{rr}(r')}, \tag{3}$$

$$\rho C' = \rho C \frac{g(r') \frac{dg}{dr'}(r')}{r'}. \tag{4}$$

K and ρC are the conductivity and density-heat capacity product of the homogeneous material, g is the reciprocal function of f (*i.e.* $g(r') = r$), $R(\theta)$ is the rotation matrix through an angle θ and R^T its transpose. The choice of the function f can lead to a cloaking device or a concentrator for instance. We chose to design a concentrator using a linear function, stretching the annular space comprised between the radii R_2 and R_3 into the annular space between the radii R_1 and R_3:

$$f(r) = \begin{cases} \dfrac{R_1}{R_2} r, & for\ r \in [0, R_2], \\ \alpha r + \beta, & for\ r \in [R_2, R_3], \end{cases} \tag{5}$$

$$\text{with } \alpha = \frac{R_3 - R_1}{R_3 - R_2} > 0 \text{ and } \beta = R_3 \frac{R_1 - R_2}{R_3 - R_2} < 0.$$

Although K' depends on r' in the area $r' \in [R_1, R_3]$, this function has the advantage to have a smaller variation of $\rho C'$ compared to a function of the type $r' = R_3(\frac{r}{R_3})^2$ used in [11, 17].

2.2. Homogenization

Since no common material has the desired anisotropic space-dependent values of $\bar{\bar{K}}'$ and $\rho C'$, we use metamaterials. The device consists of structured cells, whose effective properties correspond to the desired values. One possibility to compute the effective properties is to use the two-scale homogenization theory [11, 22], where the averaged properties of a periodic unit cell far smaller than the size of the sample are used to determine the global behavior. As the unit cell is defined in polar coordinates, it is preferable to avoid using Cartesian rectangular unit cells. To eliminate the need for a coordinate transformation between Cartesian and polar coordinates, we propose instead an original method for computing the effective thermal conductivity tensor directly in the polar system (values of K_r and K_θ) from the fluxes obtained with FE simulations.

Let us consider the unit cell of a homogeneous material depicted in Fig.1. In order to calculate K_r, we impose the following boundary conditions: $T(r = r_i) = T_i$, $T(r = r_{i+1}) = T_{i+1}$ and no flux for $\theta = \theta_1$ and $\theta = \theta_2$. In a steady state regime with no heat source, the heat equation simplifies to (no de-

pendence on θ):

$$\frac{d^2T}{dr^2} = -\frac{dT}{rdr} \tag{6}$$

The temperature is therefore given by:

$$T(r) = T(r_i) - A \cdot \ln\left(\frac{r}{r_i}\right), \tag{7}$$

with $A = \frac{T_i - T_{i+1}}{\ln\left(\frac{r_{i+1}}{r_i}\right)}$ obtained from the boundary conditions. The radial flux Φ_r is therefore:

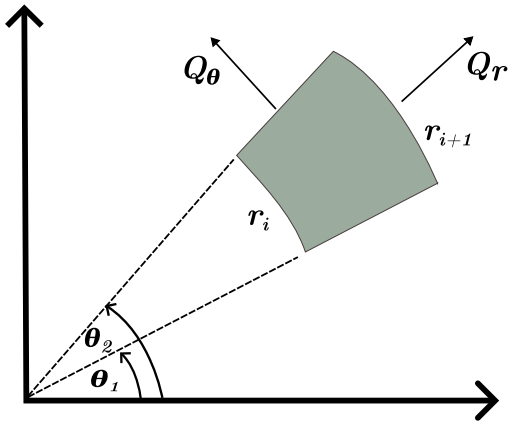

Fig. 1. Schematic representation of the heat transfer in a 2D shape cell in polar coordinates. Q_α is the integration of the flux Φ_α along the considered boundary.

$$\Phi_r = -K\frac{dT}{dr} = K\frac{A}{r}. \tag{8}$$

We can thus compute the effective radial conductivity of a structured unit cell from the average of the normal flux $\overline{\Phi_{r_i}}$ at $r = r_i$ or from the average normal flux $\overline{\Phi_{r_{i+1}}}$ at $r = r_{i+1}$:

$$K_r = \overline{\Phi_{r_i}} r_i \frac{\ln\left(\frac{r_i}{r_{i+1}}\right)}{T_{i+1} - T_i} = \overline{\Phi_{r_{i+1}}} r_{i+1} \frac{\ln\left(\frac{r_{i+1}}{r_i}\right)}{T_{i+1} - T_i}. \tag{9}$$

In the same way, to calculate K_θ, we consider the following boundary conditions: $T(\theta = \theta_1) = T_1, T(\theta = \theta_2) = T_2$ and no flux for $r = r_i$ and $r = r_{i+1}$. For a homogeneous material, the temperature does not depend on the radius r and its derivative according to θ is a constant. The integration of the azimuthal flux Φ_a along the radius is a constant Q_θ:

$$\int_{r_i}^{r_{i+1}} \Phi_a dr = \int_{r_i}^{r_{i+1}} -K\frac{\partial T}{r\partial\theta} = -K\left[\frac{\partial T}{\partial\theta}\ln(r)\right]_{r_i}^{r_{i+1}} = Q_\theta \tag{10}$$

The temperature follows a linear relationship with θ:

$$T(\theta) = T_1 + \frac{\partial T}{\partial\theta}\cdot(\theta - \theta_1) = T_1 + \frac{Q_\theta}{K \cdot \ln\left(\frac{r_i}{r_{i+1}}\right)}\cdot(\theta - \theta_1) \tag{11}$$

The T_2 boundary condition provides the relationship between Q_θ and the other parameters. Consequently, the effective azimuthal conductivity of a structured unit cell can be determined based on Q_θ (which can be obtained through FE simulations on either boundary $\theta = \theta_1$ or $\theta = \theta_2$):

$$K_\theta = Q_\theta \frac{(\theta_2 - \theta_1)}{(T_2 - T_1).\ln\left(\frac{r_i}{r_{i+1}}\right)} \tag{12}$$

For the background cells, which are in the Cartesian system, the conductivity is derived from the same methodology. For K_w (where w represents either x or y), we apply the Dirichlet condition with the temperature T_0 for $w = 0$ and T_1 for $w = a$, with a the cell's period. For the other two boundaries, we use the Neumann conditions (no flux). K_w is then determined according to the formula $K_w = abs(flux/(T_0 - T_1) * a)$, where *flux* is the average of the heat flux at one of the Dirichlet boundaries and $abs()$ is the absolute value function. In our designs, x and y play the same role within the background cells.

The effective density-heat capacity product depends on the frequency. Indeed, in a structured design, the thermal resistance to reach some component can be higher compared to other components (for instance, some metal surrounded by insulating material will take longer to heat than the rest of the device). However, if in the considered time scale, there is sufficient heat flow between all the conductive material parts to establish a pseudo equilibrium, this effective parameter can be approximated by taking the surface average of the density-heat capacity product for unit cells in the 2D design, for the unit cells in the 3D design, by multiplying the metal ρC value and the ratio between the volume of metal (including the metal above the unit cell) and the volume of the 3D unit cell. This implies that no conductive material should be entirely surrounded by insulating material.

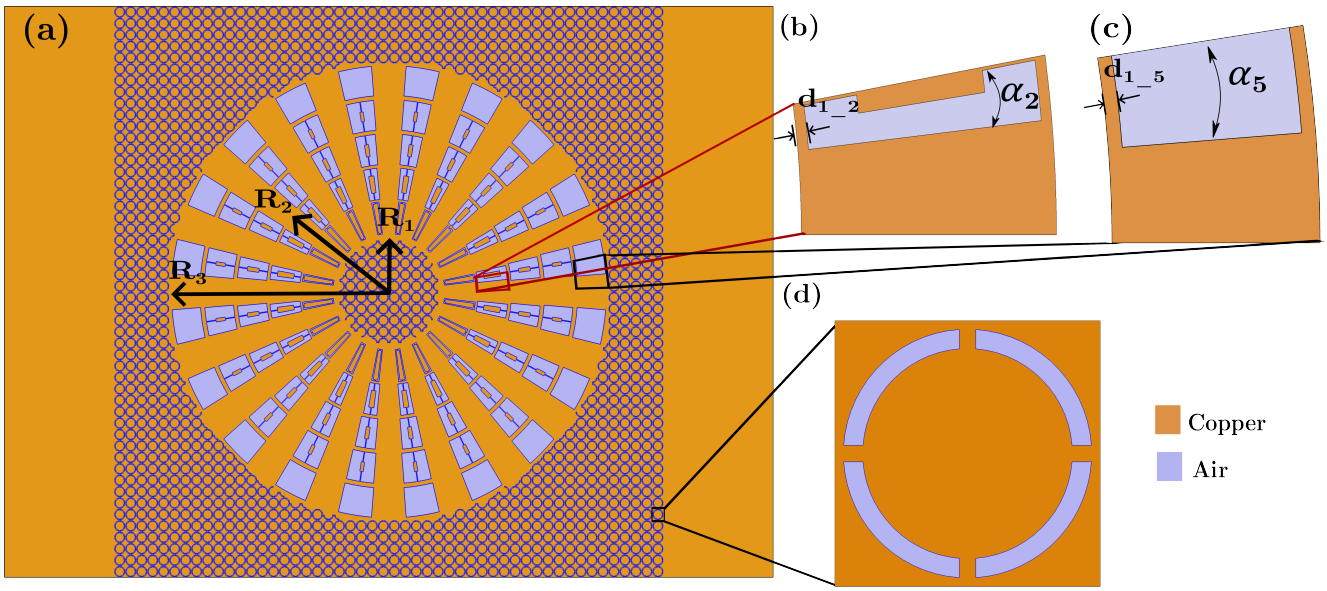

Fig. 2. (a) 2D thermal concentrator design. Note that the radius R_2 corresponds to a radius in the homogenous isotropic material which is mapped into the radius R_1 in this design

. Half of the concentric area's second layer (b) and fifth layer unit-cells (c). (d) Background medium unit-cell.

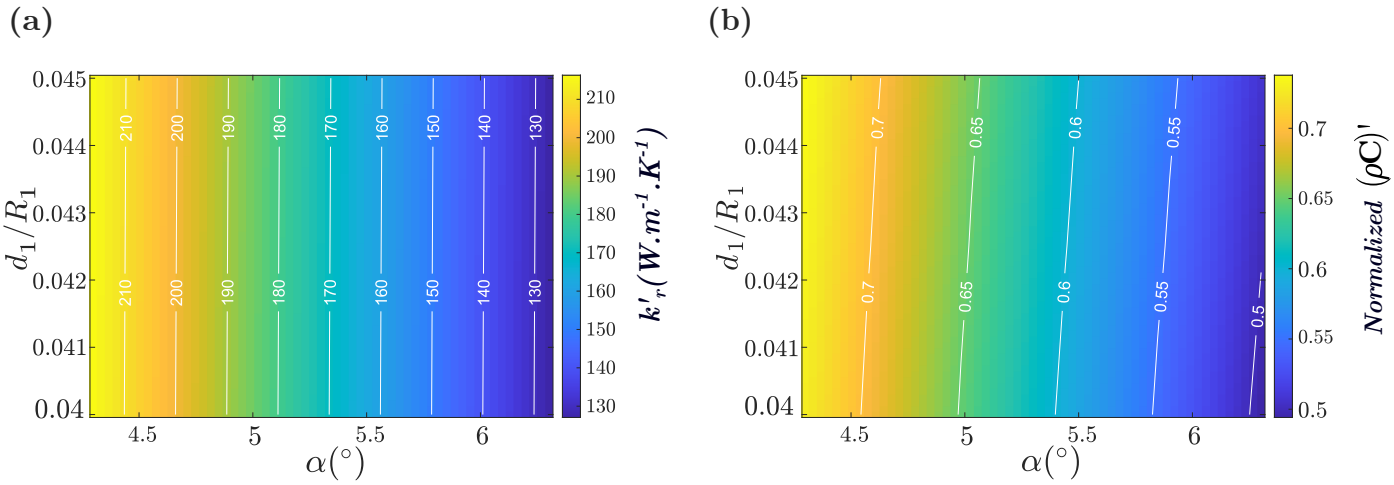

Fig. 3. Design targets K'_r (a) and normalized $(\rho C)'$ (b) for the outer cell according to the design variables d_1/R_1 and α

2.3. Design

2.3.1. 2D Design

For our demonstrator, we have designed a heat flux concentrator where $R_2 = 2R_1$ and $R_3 = 4R_1$. The temperature that would normally be at $r = R_2$ in a homogeneous material is instead found at $r = R_1$, concentrating the heat flux towards the center. For practical purposes, as a trade-off between precision and ease of fabrication, the annular space between R_1 and R_3 is divided in 5 radial layers and 20 tangential sectors, as shown in Fig.2a. The disk of radius R_1, where should be some useful energy harvester, is left as the background medium. For the conductive material, we have chosen copper ($K_{metal} = 400\ W \cdot m^{-1} \cdot K^{-1}, \rho C_{metal} = 3.44 \times 10^6\ J \cdot K^{-1} \cdot m^{-3}$), while air is chosen as the insulating material ($K_{ins} \sim 0.026\ W \cdot m^{-1} \cdot K^{-1}, \rho C_{ins} = 1212\ J \cdot K^{-1} \cdot m^{-3}$).

As a unit cell of the metamaterial of the annular space, we have chosen to fill it with the conductive material with a hole in the center (rectangle deformed to follow the polar coordinates) as seen in Fig. 2c. In the case of multiple cells, it can also

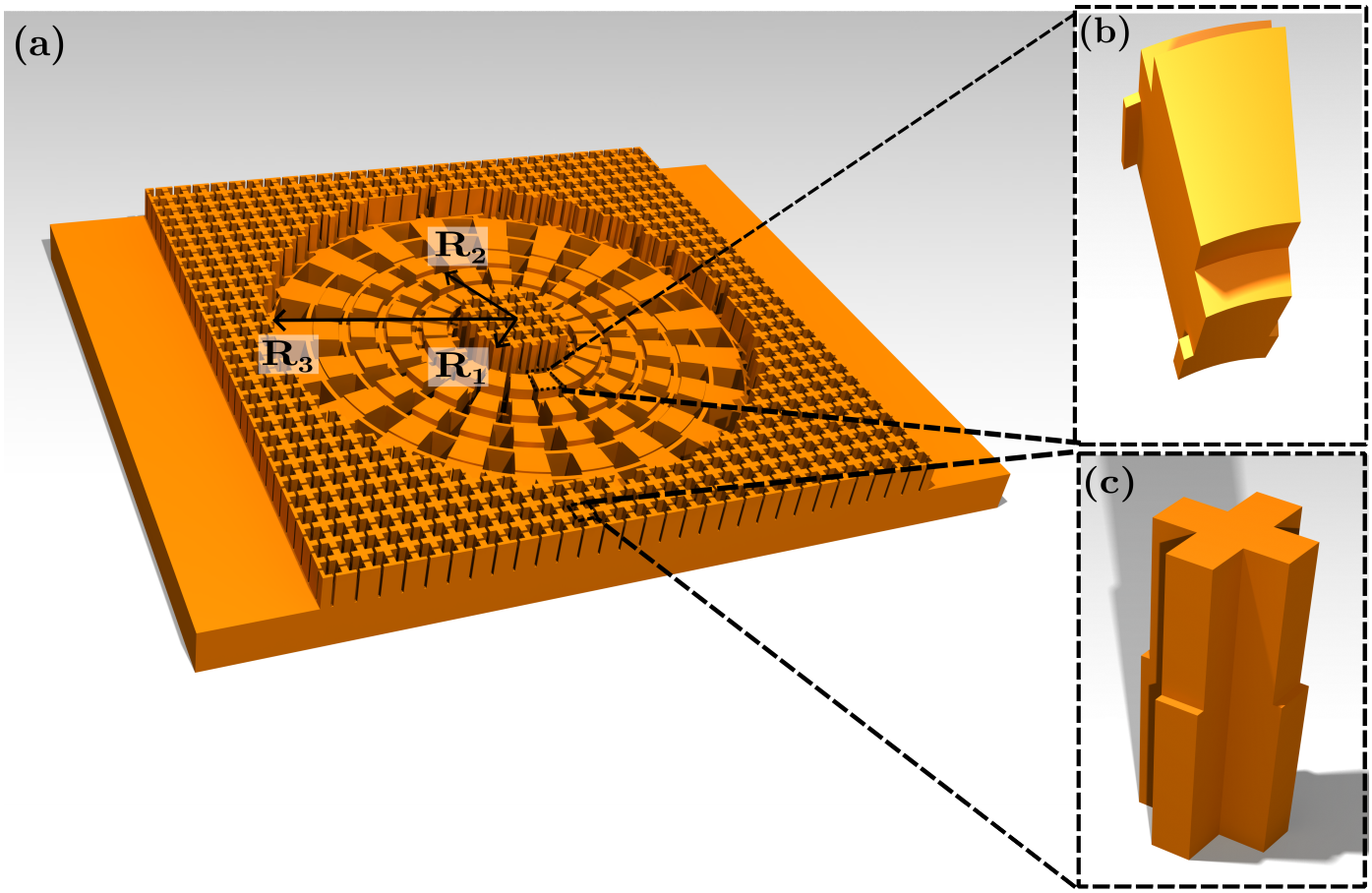

Fig. 4. (a) 3D thermal concentrator design. Note that the radius R_2 corresponds to a radius in the homogenous isotropic material which is mapped into the radius R_1 in this design

. (b) Concentric area's second layer unit-cell (c) Background medium unit-cell.

be viewed as a unit cell filled with the insulating material with a conductive cross (deformed to follow the polar coordinates). As shown with Fig. 3a, the radial conductivity K'_r depends mainly on the angle α defining the size of the insulating material. In other words, it depends mainly on the width of the radial arm. Since the width of the azimutal arm d_1 is much smaller (as K'_θ is much smaller than K'_r), the azimutal conductivity K'_θ depends strongly on d_1 but α also plays a significant role (see Fig. 3b). We adjust (increase) the $\rho C'$ value by incorporating metal inside the insulating area (cf. fig. 2b). As it is mostly surrounded by insulating material, the metal will hardly contribute to the conduction process but nonetheless increase the heat needed to increase the temperature. However, as mentioned earlier at the end of the homogenization section, this metal part should be connected to the rest of the metal. Hence, we utilize bridges in the radial direction, which is the main direction of the heat flux (cf. Fig. 2b). Adding this metal has a small influence on the effective conductivity tensor and must be taken into account. The background is also constituted of a metamaterial in order to achieve an isotropic thermal conductivity of a third of the conductive material (k_b = 133 $W.m^{-1}.K^{-1}$). The unit cell is filled with a conductive material that has a circular hole of insulating material. The ρC value of the background is increased and adjusted so that the outward cell of the annular space has no metal inside the insulating area. To increase the ρC value of the background, a metallic disk is inserted inside the insulating area and connected to the rest of the metal with four bridges (cf. Fig. 2d). Figure 6a) shows the obtained normalized values of ρC for the five unit cells of the concentrating area and compares them to the ideal values according to the radial position. Additionally, for comparison, it also shows the values of a design

using the same linear function that only considers the anisotropic conductivities and not the position-dependent density – heat capacity product.
Although functional (see paragraph results and discussions), this design can be rather challenging to fabricate with sufficient thickness to minimize the air convection effect if not under vacuum. Another possibility is to use the third dimension which is nowadays easily accessible through 3D printing.

2.3.2. 3D Design

We have therefore also developed a 3D concentrator design. The heat flow is still predominantly two-dimensional but the third dimension allows for more flexibility in the lateral dimensions. In this design, we have introduced metal components on top of the metal connections, varying their thickness, rather than incorporating metals within the insulating area. The added material on the top of one cell does not directly connect to the material added on the top of another cell: this, therefore, limits its influence on the anisotropic conductivities but still has to be considered. The overall lateral dimensions of this design are 60×70 *mm*, with $R_1 = 6$ *mm*, $R_2 = 12$ *mm*, and $R_3 = 24$ *mm*. The thickness of the border parts (also corresponding to the unit cells thickness used to compute the homogenized ρC) is 4 *mm*. Once again, as a trade-off between precision and ease of fabrication, the annular space between R_1 and R_3 is divided into 5 radial layers and 20 tangential sectors, as depicted in Fig. 4a. We also used copper as the conducting material. The insulating material (air) is considered negligible, therefore the thermal conductivity of the metal does not influence the design but has an effect on the time scale and the sensitivity to the air convection effect. To achieve an isotropic thermal conductivity that is one-third of the conductive material for the background in the 3D device, we used a metamaterial. The unit cell of the metamaterial consists of the conductive material filled with an insulating material in the shape of a square hole, with a periodic structure. Another way to consider the cell is by shifting it by half a period in both directions, resulting in a metal cross shape. We increased and adjusted the ρC value of the background cell so that the outer cell of the concentrating part does not need adjustment of its ρC value. We achieved this by introducing a metal cross on the top (when defining the cell as a cross), with arms shorter than the period to ensure they do not touch the other cells, as illustrated in Fig. 4c. Equivalently, it can be seen as adding metal L-shaped parts on top when defining the cell as a square with a hole in the middle. In the concentrating area, similarly to the 2D design, the cells can be viewed as metal crosses (deformed by the polar geometry) where the longitudinal arm is wider than the azimuthal one because the conductivity is larger in this direction. For the inner cell of the concentrating area, in order to have an azimuthal arm wide enough for fabrication, we reduced its thickness (cf. Fig. 4b). We increased and adjusted the ρC values by adding bumps on the top of the radial arm, not touching the bumps of the other cells (in order to greatly reduce the increase of K_r introduced by these bumps). Figure 7a presents the obtained ρC values for the five cells in the concentrating area compared to the ideal value according to the radial position.

2.4. Fabrication

We fabricated our 3D design by utilizing 3D metal printing (cf. Fig 5). Copper was selected because it has high thermal conductivity. The thickness needed to limit the air convection effect is thus reduced. For the Laser Power Bed Fusion (LPBF) machine, we use a machine from the Trumpf company: the TruPrint 1000 Green Edition which enables 3D printing of materials such as copper. It works with a green laser at 515 *nm* with a maximum power of 500 *W* and a beam diameter of 200 μm. The level of oxygen in the fabrication chamber was the lowest possible on the machine: 100 *ppm* (under an argon atmosphere). We use a soft silicone scraper to spread the powder and the layer thicknesses are 30 μm. We operate with the standard parameters of the machine for pure copper making it possible to obtain a density of 99.9% and an electrical conductivity of 101% International Annealed Copper Standard (IACS), which means the thermal conductivity of the copper was set up $\simeq 400\ W \cdot m^{-1} \cdot K^{-1}$. The laser power was 485 *W* with a velocity of 600 mm/s and a hatch distance of 120 μm. The base plate is a stainless steel ($316L$) disk.

First, we made 3 small parts with different compensation distances (150, 190, and 230 μm). The

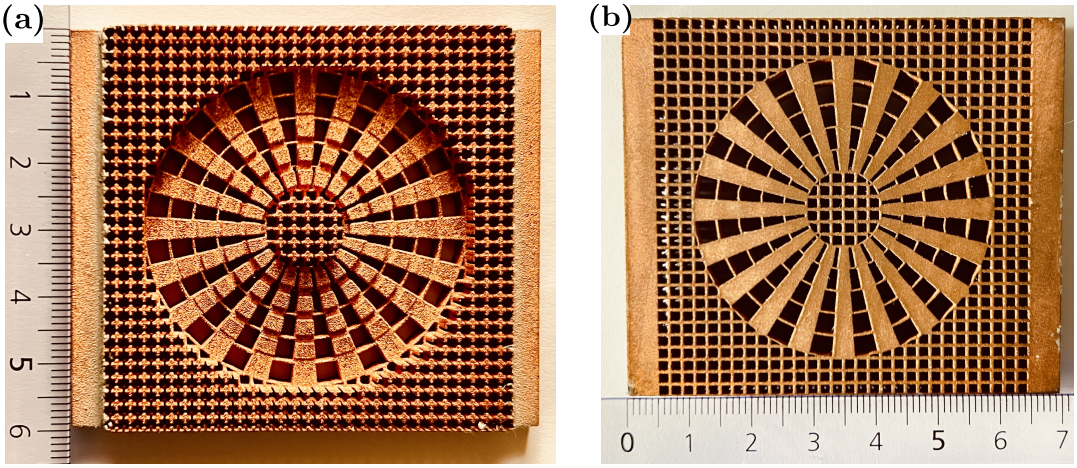

Fig. 5. Fabricated thermal concentrator by metal 3D printing

compensation distance is the distance between the edge of the part and the center of the laser line. When this compensation distance increases, it decreases the thickness of the part. For the final part, a compensation distance of 210 µm was adopted.

2.5. Characterization

The 2D design was not fabricated but simulations were performed using the commercial software COMSOL Multiphysics, providing an insight of its behavior. The overall lateral dimensions are 20×28 *mm* with $R_3 = 8$ *mm* and the thickness is 500 μm. The air convection effect has been taken into account with a coefficient $h = 15\ W \cdot m^{-2} \cdot K^{-1}$ on one side which corresponds to the established value in our previous work [17]. The radiation loss has also been included. The boundary conditions on the left and right borders are fixed temperatures at 64 ^oC and 4 ^oC, respectively. For the time evolution simulation, the initial temperature of the device is at room temperature, 23 ^oC.

To characterize the 3D design, we employed a similar setup to the one used by Ji *et al*. [17]. To achieve a nearly constant temperature on the hot side, we used a regulated hot plate with an aluminum block placed on it. On the cold side, our device was positioned on an aluminum block immersed in an ice-cold water bath. We enhanced the thermal contact by applying a thermal paste between the aluminum blocks and our device. To measure the temperature profile using Planck thermal emission, we used a highly sensitive and large dynamics (14 bits) infrared thermal camera (FLIR A6702sc) to capture thermal images and movies. Since the additional components used to increase the ρC value would also increase the air convection effect and act as heat radiators (cf. Fig 5a), we covered it with a polystyrene block. The thermal measurements were performed from the other side (flat side). Furthermore, we applied dark tape to this side to reduce reflection and increase emissivity. We compared these measurements with simulations carried out using the commercial software COMSOL multiphysics. The thermal paste was included in the simulation of an ideal concentrator and its thickness was adjusted to match temperatures on the device sides with the experimental ones.

3. Results and discussions

3.1. 2D design

As previously mentioned, our method enables us to obtain the desired local ρC values as depicted in Figure 6a. We also obtained the desired anisotropic thermal conductivities, which control the steady-state heat fluxes and temperature distribution. Figure 6b illustrates the simulated steady-state temperature distribution for both the ideal case (that is to say the perfect anisotropic non-structured result of the coordinate transformation) and the 2D design. In the concentrating section, the iso-temperature lines are stretched towards the center, indicating the concentration of the heat flow. The ones of the 2D design are distorted due to the alternating arrangement of conducting and insulating materials, as observed

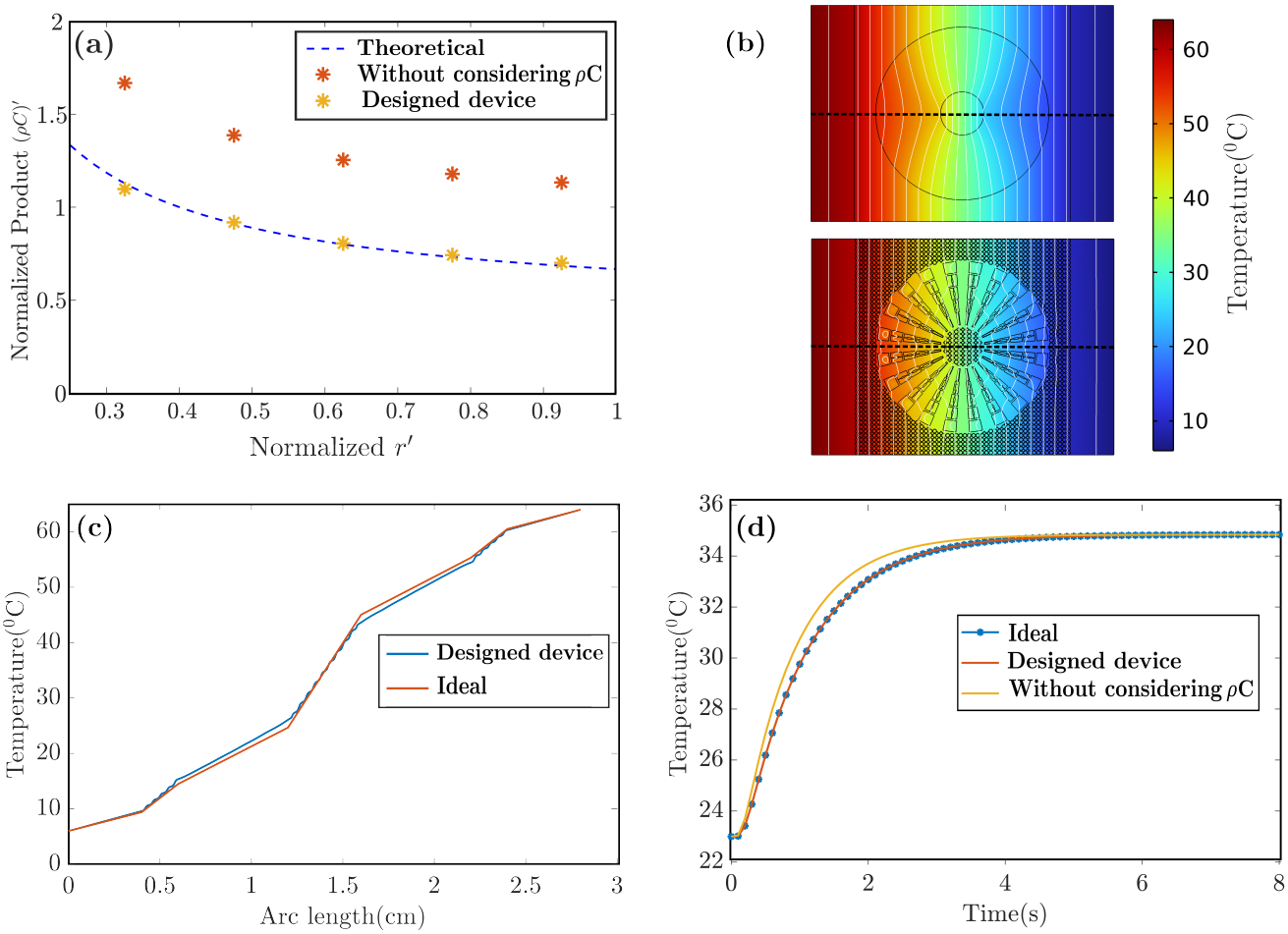

Fig. 6. Simulation comparisons between the 2D design and the ideal concentrator. The air convection is included. (a) ρC value versus the radial position. (b) The steady-state temperature of the 2D design (bottom) compared to the ideal case (top). The white lines denote temperature iso-temperature lines. The black dash line denotes the observation line for Fig 6.c. (c) Steady-state temperature evaluation of the device along the observation line. (d) Time evolution of the temperature in the middle of the devices for the ideal one, the 2D design and a concentrator designed without taking into account ρC.

in a previous study[17]. To reduce this effect, the size of the metamaterial cells should be reduced. To facilitate the comparison between the ideal concentrator and the 2D design, a cut line passing through the middle has been traced. In figure 6c, we plotted the steady state temperature of our design and of the ideal case along this cut-line. It clearly demonstrates a very good agreement between the two designs, albeit with some discrepancies attributed to the influence of the air convection. Indeed, when removing the air convection effect in the simulation or increasing the thickness, the two curves nearly overlap each other. An original aspect of our work is that we considered the modification of the density-heat capacity product. This material property does not affect the steady-state heat equation but is crucial in the temporal one. Figure 6d shows the simulated temporal evolution of the temperature at the center of the device for the ideal concentrator and our design when the hot and cold boundary conditions follow a Heaviside function (multiplied to obtain the previous boundary temperatures), with the initial temperature set as the room temperature. The two curves are nearly the same. For comparison purpose, the temperature evolution for a design not taking into account ρC is also plotted. It highlights the advantage of our design compared to previous ones to respect correct time evolution.

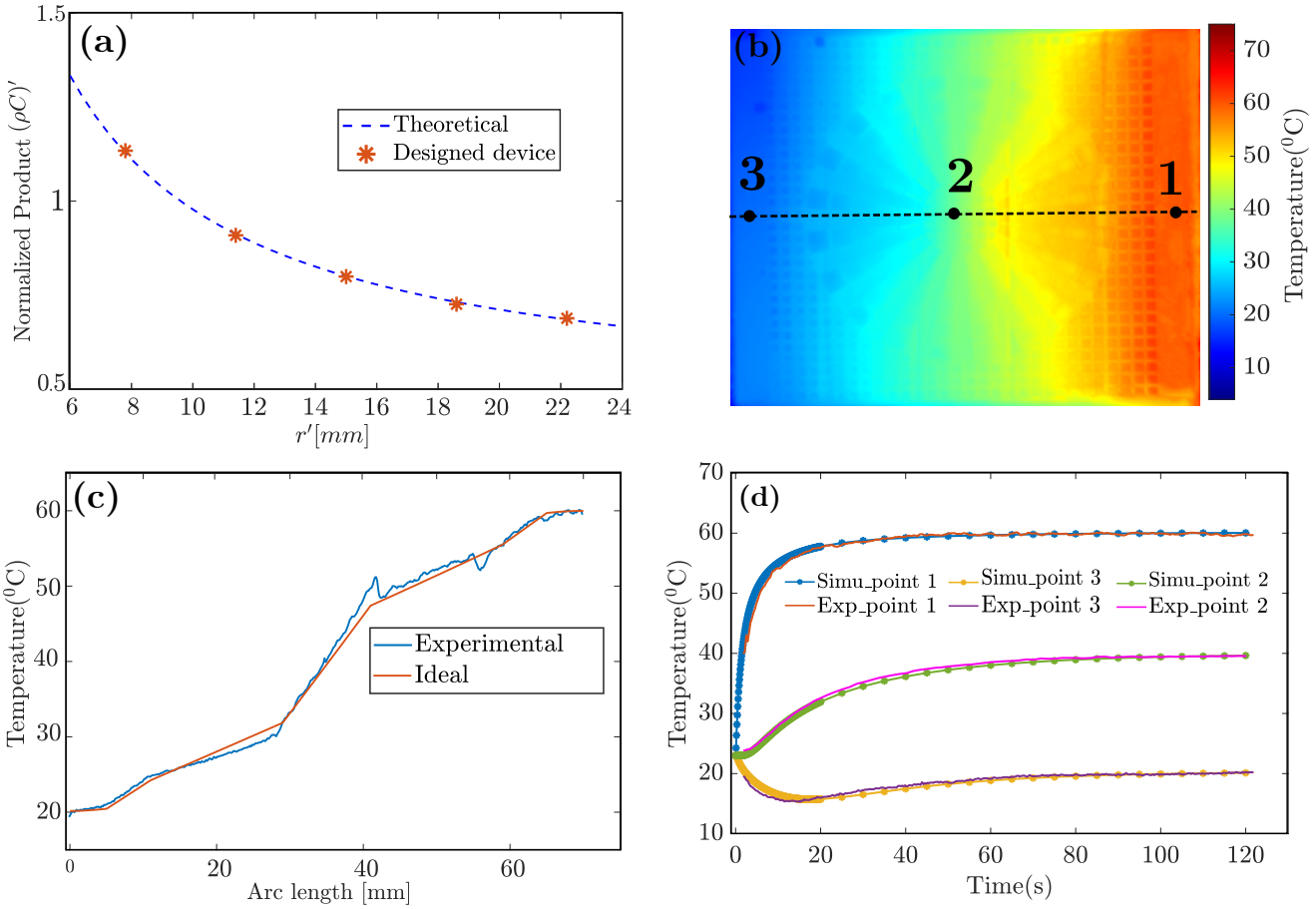

Fig. 7. 3D design experimental results compared with simulations. (a) Comparison of theoretical and design's ρC value according to the radius r'. (b) Experimental thermal image of the device taken after the steady-state regime was reached. The black dashed line denotes the observation line and the black dots are the points for time evaluation. (c) Experimental and simulated steady-state temperature along the observation line. (d) Experimental and simulated time evolution of the temperature for the 3 points defined in (b)

3.2. 3D design

Figure 7a demonstrates that our 3D design enables us to obtain the desired local ρC values. Figure 7b presents the experimental surface temperature of the flat side of the device after reaching the steady-state regime. It matches the desired mapping of the ideal case (see Fig. 6b). In Figure 7c, we plotted the experimental and simulated ideal steady-state temperature along a cut-line defined in Figure 7b. Like the 2D design, the two curves are similar and the differences are partially attributed to air convection and radiation. According to our simulations, the heat transfer is predominantly driven by conduction, accounting for approximately 87% of the total heat exchange, complemented by a contribution of roughly 9% from air convection, while radiation plays a minor role at 4%. When the device was removed, we measure the temperature of the air at its original location. These measurements indicated a temperature gradient between the hot and cold sides. While the impact was minor, our simulations include this gradient for air convection and radiation. During the experiment, the temperature of the cold side boundary was not constant. This can be attributed partly to the thermal resistance between the cold bath and the device, despite the use of thermal paste. It also may come from the lack of stirring in the cold bath. As mentioned in the characterization section, the thickness of the thermal paste on both sides was adjusted in the simulation to obtain a time evolution of the boundaries temperature similar to the experimental ones. Figure 7c shows the experimental and simu-

lated steady-state temperature of the ideal concentrator along the observation line defined in 7b. There is a good agreement between the experimental and simulated curves, denoting the expected behaviour of our device. The increase of the slope in the middle area demonstrates the concentrating effect of our device. Figure 7d presents the experimental and simulated time evolution of the temperature for the 3 points defined in Figure 7b. Once again, the experimental curves closely match the simulated ones for an ideal concentrator. This demonstrates that a metamaterial not only enables the achievement of the right anisotropic thermal conductivity but also the desired local density – heat capacity product.

4. Conclusion

We have successfully designed two thermal concentrators: a 2D design featuring uniform thickness and a 3D design (with predominantly 2D heat flow). These designs were developed based on the principles of coordinate transformation and metamaterials. By structuring the thermal conductor, we achieved the desired local anisotropic thermal conductivities and density-heat capacity products (ρC). For the 2D design, both steady-state and time-dependent simulations demonstrate that the 2D device performs as expected.

The 3D concentrator was manufactured using 3D metal printing and characterized using a thermal camera to analyze its steady-state and time evolution characteristics. The experimental behaviors closely match those of the simulated ideal concentrator. This demonstrates that not only a metamaterial can achieve the correct anisotropic thermal conductivity but also the desired local density – heat capacity product. This method can also be applied to the design of thermal cloaks (invisibility cloak for heat conduction for stealth applications for instance) or any other heat flux manipulation where both anisotropic K and ρC must be locally adjusted. Whether in steady state, harmonic or time-dependent cases, small perturbations next to the device would unfortunately be seen. However, they would decrease as the distance from the device increases or as the unit cells of the metamaterial become smaller.

Declaration of Competing Interest

The authors declare that they have no known competing financial interests or personal relationships that could have appeared to influence the work reported in this paper.

Acknowledgments

We thank Julio Andrés Iglesias Martinez for giving helpful advises for this work. This work was supported by the EIPHI Graduate School (grant number ANR-17-EURE-0002) and the French "Investissements d'Avenir" program, project ISITE-BFC (contract ANR-15-IDEX-0003). The authors acknowledge the support of the French RENATECH network.

References

[1] V. Veselago, L. Braginsky, V. Shklover, C. Hafner, Negative refractive index materials, Journal of Computational and Theoretical Nanoscience 3 (2) (2006) 189–218.

[2] N. Kaina, F. Lemoult, M. Fink, G. Lerosey, Negative refractive index and acoustic superlens from multiple scattering in single negative metamaterials, Nature 525 (7567) (2015) 77–81.

[3] X. Ren, R. Das, P. Tran, T. D. Ngo, Y. M. Xie, Auxetic metamaterials and structures: a review, Smart materials and structures 27 (2) (2018) 023001.

[4] F. Monticone, A. Alu, Metamaterial, plasmonic and nanophotonic devices, Reports on Progress in Physics 80 (3) (2017) 036401.

[5] J.-P. Groby, N. Jiménez, V. Romero-García, Acoustic metamaterial absorbers, Acoustic Waves in Periodic Structures, Metamaterials, and Porous Media: From Fundamentals to Industrial Applications (2021) 167–204.

[6] R. Schittny, M. Kadic, S. Guenneau, M. Wegener, Experiments on transformation thermodynamics: molding the flow of heat, Physical review letters 110 (19) (2013) 195901.

[7] S. Guenneau, C. Amra, D. Veynante, Transformation thermodynamics: cloaking and concentrating heat flux, Optics Express 20 (7) (2012) 8207–8218.

[8] S. Narayana, Y. Sato, Heat flux manipulation with engineered thermal materials, Physical review letters 108 (21) (2012) 214303.

[9] D. Petiteau, S. Guenneau, M. Bellieud, M. Zerrad, C. Amra, Spectral effectiveness of engineered thermal cloaks in the frequency regime, Scientific reports 4 (1) (2014) 7386.

[10] Q. Ji, X. Chen, G. Fang, J. Liang, X. Yan, V. Laude, M. Kadic, Thermal cloaking of complex objects with the neutral inclusion and the coordinate transformation methods, AIP Advances 9 (4) (2019).

[11] Q. Ji, X. Chen, J. Liang, V. Laude, S. Guenneau, G. Fang, M. Kadic, Designing thermal energy harvesting devices with natural materials through optimized microstructures, International Journal of Heat and Mass Transfer 169 (2021) 120948.
[12] Y. Li, X. Shen, Z. Wu, J. Huang, Y. Chen, Y. Ni, J. Huang, Temperature-dependent transformation thermotics: from switchable thermal cloaks to macroscopic thermal diodes, Physical review letters 115 (19) (2015) 195503.
[13] M. Lei, C. Jiang, F. Yang, J. Wang, J. Huang, Programmable all-thermal encoding with metamaterials, International Journal of Heat and Mass Transfer 207 (2023) 124033.
[14] M. Raza, Y. Liu, E. H. Lee, Y. Ma, Transformation thermodynamics and heat cloaking: a review, Journal of Optics 18 (4) (2016) 044002.
[15] S. Yang, J. Wang, G. Dai, F. Yang, J. Huang, Controlling macroscopic heat transfer with thermal metamaterials: theory, experiment and application, Physics Reports 908 (2021) 1–65.
[16] X. Yue, J. Nangong, P. Chen, T. Han, Thermal cloak: Theory, experiment and application, Materials 14 (24) (2021) 7835.
[17] Q. Ji, X. Chen, J. Liang, G. Fang, V. Laude, T. Arepolage, S. Euphrasie, J. A. I. Martinez, S. Guenneau, M. Kadic, Deep learning based design of thermal metadevices, International Journal of Heat and Mass Transfer 196 (2022) 123149.
[18] F. Chen, D. Yuan Lei, Experimental realization of extreme heat flux concentration with easy-to-make thermal metamaterials, Scientific reports 5 (1) (2015) 11552.
[19] G. Park, S. Kang, H. Lee, W. Choi, Tunable multifunctional thermal metamaterials: manipulation of local heat flux via assembly of unit-cell thermal shifters, Scientific reports 7 (1) (2017) 41000.
[20] W. Sha, R. Hu, M. Xiao, S. Chu, Z. Zhu, C.-W. Qiu, L. Gao, Topology-optimized thermal metamaterials traversing full-parameter anisotropic space, npj Computational Materials 8 (1) (2022) 179.
[21] T. Sun, X. Wang, X. Yang, T. Meng, R. He, Y. Wang, Design of thermal cloak and concentrator with interconnected structure, International Journal of Heat and Mass Transfer 187 (2022) 122568.
[22] G. Allaire, Homogenization and two-scale convergence, SIAM Journal on Mathematical Analysis 23 (6) (1992) 1482–1518.